ORIGINAL PAPER

Design Considerations for Controlling Silicon Nanoparticle Nucleation and Growth in a Nonthermal Plasma

Eric Husmann[1] · Jordyn Polito[2] · Steven Lanham[2] · Mark J. Kushner[2,3] · Elijah Thimsen[1,4]

Abstract

Controlling the nucleation and growth of nanoparticles in low temperature plasma systems is imperative for controlling nanoparticle size distributions; and for some applications such as deposition and etching in microelectronic processing, preventing particle contamination. In this work, silicon nanoparticle (NP) production from silane is used as a model system to investigate the nucleation process. Although the mechanisms responsible for silicon NP nucleation and growth have been studied, it is unclear how controllable system parameters (e.g., pressure, system geometry, and gas composition) can be used to inhibit or promote NP formation. For example, the transport of reactive silane species is expected to significantly affect the feed fraction of silane required to nucleate silicon NP (the nucleation onset fraction) due to losses at the reactor walls. In this work, NP mass density was determined as a function of system pressure, gas composition, and reactor diameter for a tubular flow-through radiofrequency plasma using $Ar/H_2/He/SiH_4$ gas mixtures. A quartz crystal microbalance impactor was developed to measure the total aerosol mass density downstream of the plasma and thereby identify the nucleation onset and its dependence on process parameters. A reaction mechanism was developed and incorporated into a global plasma chemistry model to better understand the nucleation onset and NP growth.

✉ Elijah Thimsen
elijah.thimsen@wustl.edu

1   Department of Energy, Environmental and Chemical Engineering, Washington University in St. Louis, St. Louis, MO 63130, USA

2   Department of Chemical Engineering, University of Michigan, Ann Arbor, MI 48109, USA

3   Department of Electrical Engineering and Computer Science, University of Michigan, Ann Arbor, MI 48109, USA

4   Institute for Materials Science and Engineering, Washington University in St. Louis, St. Louis, MO 63130, USA

Introduction

The promotion or suppression of silicon nanoparticle formation in dilute silane containing plasmas is a topic of interest within the nanomaterials field. Silicon nanoparticles are being investigated for their use in photocatalysis [1, 2], optoelectronics [3], energy storage [4], and medicine [5, 6]. Controlling the nucleation and growth rate of nanoparticles allows for increased particle mass yields, control over particle size, or even suppressed particle formation if particles are undesired. In the case of semiconductor processing, particle deposition onto microelectronics devices during fabrication steps using plasmas continues to be a source of reduced yields [7]. With device dimensions having approached nm scale, particles below 10 nm in diameter are "killer defects" [8]. The suppression of particle formation in these systems typically is accomplished by reducing plasma power, which reduces processing rates and utilization of the feedstock gases. As such, the ability to suppress particle formation while promoting film growth or etching is of great benefit.

Several methods have been reported to reduce particle contamination of thin films during plasma processing. The methods used to prevent existing particles from reaching a film surface include increasing the volumetric flowrate through the plasma reactor to sweep out particles [9] and leveraging thermophoresis to transport particles away from a higher temperature substrate [10]. Plasma pulsing has also been shown to be capable of reducing particle formation and/or removing electrostatically trapped particles [11–14]. Silane containing plasmas for silicon amorphous film deposition are often diluted with hydrogen to improve film quality [15, 16], a practice that has also been shown to inhibit particle formation [14, 17]. As a side effect, hydrogen dilution can also decrease film deposition rates [18]. In spite of these techniques, particle contamination remains a significant problem and is made more challenging by the need to prevent formation of particles less than 10 nm in diameter to meet current process requirements. Methods of in-situ detection of small densities of particles less than 10 nm in diameter are required to ensure that state-of-the-art semiconducting processing reactors operate at acceptably low levels of particle contamination.

A variety of commercially available instruments can be used for the in-situ detection and quantification of aerosol nanoparticles including: scanning mobility particle sizers (SMPSs) [19], electrical low pressure impactors (ELPIs) [20], and micro-orifice uniform deposit impactors (MOUDIs) [21]. These devices are well suited for sampling aerosols at atmospheric pressure where the gas density is high. For these conditions, ELPIs can detect particles below 10 nm in diameter. However, most semiconductor processing reactors and low temperature plasma reactors operate at pressures in the range 10^{-3} to 10 mbar. Diagnostic methods suitable for atmospheric or low pressure sampling include optical particle spectrometers (OPCs) [22, 23] and aerosol mass spectrometers (AMSs) [24–26]. OPCs are suitable for detecting particles above 70 nm in size [22], and AMSs can detect particles down to about 10 nm in size [24]. Although each of these devices are powerful, robust and cost-effective techniques to detect low concentrations of aerosol particles below 10 nm in size under low pressure conditions are still needed.

In this paper, we discuss the development and application of a quartz crystal microbalance (QCM) impactor capable of detecting nanoparticles having sizes 10 nm or less under low pressure conditions. Although size information cannot be obtained directly from the diagnostic reported herein, there are significant benefits of using a single impaction stage including: high mass resolution, high mass sensitivity, low capital cost compared to other instruments, and low operating expenses. For applications such as monitoring dust contamination in microelectronic processing reactors, size information is not always

important since the goal is often to suppress nanoparticle formation, or more specifically, have the mass density of the aerosol below a certain value defined by the process quality control constraints. As a demonstration of the capabilities of this QCM impactor, we explored silicon nanoparticle nucleation from silane in a low temperature plasma reactor, and processes that contribute to the nucleation of such particles.

In spite of several studies related to the nucleation and formation of silicon nanoparticles in dilute silane plasmas, little focus has been given to suppressing or promoting particle formation by exploiting the transport of reactive silane radical species. Maemura et al. studied particle densities in a parallel plate plasma reactor at two different electrode spacings; however, the effects of electrode spacing on particle mass density were unclear [27]. Bhandakar et al. demonstrated that particle formation can be suppressed by increasing the Brownian diffusion of reactive species by increasing the bulk gas temperature [28].

In this work, a QCM impactor was developed to study the effects of tube diameter, reactor pressure, and gas composition on particle formation (presented as a mass density of particles leaving the plasma reactor). Decreasing the discharge tube diameter inhibited particle formation as reactive species diffuse shorter distances on average to be lost to the reactor walls. Since diffusion coefficients scale inversely with pressure, to test the hypothesis we showed that increasing pressure can also promote particle formation by suppressing diffusive losses. As hydrogen addition to the gas mixture is known to inhibit particle growth, hydrogen content in the reactor inlet was also varied to determine if the consequences of hydrogen content and tube diameter/operating pressure are cumulative. A 0-dimensional global plasma chemistry model was adapted to predict NP growth, and to provide further insights into silicon nanoparticle growth as a function of inlet gas composition and reactor diameter.

Methods

To quantify the effects of pressure, reactor tube diameter, hydrogen content, and the silane fraction fed on NP nucleation, experiments were performed for two sets of conditions: constant pressure, and constant reactor tube diameter. For each of these cases, hydrogen content and the silane fraction were varied, however, the total molar flowrate was constant for all experiments. Particles generated in the plasma reactor were detected by the QCM impactor. Comparison of trends for NP production were made with results from the global plasma chemistry model.

Experimental Methods

The primary components of the experimental setup are the tubular plasma reactor and the QCM impactor, illustrated in Fig. 1. The plasma reactor consists of a 25 cm-long fused silica tube with two ring electrodes to produce a capacitively coupled plasma (CCP). Tubes having inner diameters of 1.0 cm, 1.7 cm, 2.2 cm, and 3.2 cm were investigated. Further details on the reactor geometry can be found in section S.1 of the Supplemental Information (SI). The feed gas was 0.9% silane in helium and a balance gas of either pure argon, 10% hydrogen in argon, or pure hydrogen. The total molar flowrate, controlled by flow controllers (MKS Instruments and Bronkhorst), of the feed gas was held constant at 52 standard cubic centimeters per minute (sccm). The reactor pressure was varied from 4.5 to 8.5 Torr by throttling the pump via a valve. A radio frequency (RF) 13.56 MHz AG0163
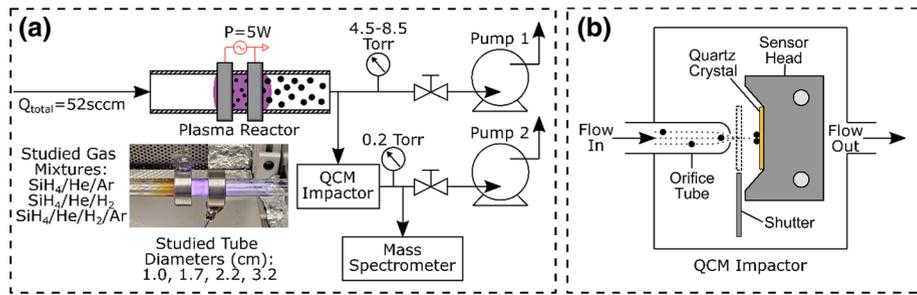
Fig. 1 **a** Schematic of the experimental apparatus **b** diagram of the QCM impactor

power supply with an AIT600 matching network (T&C Power Conversion) was used to supply the plasma reactor with 5 W of power, which was constant for all conditions. Ideally, average plasma parameters (e.g., electron temperature, ion density, bulk gas temperature) would be kept constant for all conditions; however, the measurement and maintenance of these parameters was beyond the scope of this work. Note that the measurement of plasma parameters for a silane plasma using Langmuir probe techniques [29] is made challenging due to silicon deposition fouling on the probe tips [30].

Downstream of the plasma reactor, gas was diverted to the QCM impactor. The amount of gas diverted was not held constant due to the different reactor pressures and chemical composition. A 150 μm diameter orifice tube (Lenox Laser) was used to impact particles onto the quartz crystal (Telemark, part number 880-0201-3). Molar flowrates to the QCM were determined using software provided by the orifice manufacturer [31]. The pressure downstream of the orifice was held at 0.2 Torr.

For the conditions of this investigation, all particles, irrespective of size, are expected to impact onto the quartz crystal since the critical cutoff diameter of impaction, $d_{p,c}$, was always less than 1 Å (much smaller than any critical cluster size). As a result, the QCM measures the total aerosol mass current in the sample stream. The cutoff diameter of impaction is given by [23]:

$$d_{p,c} = \left(\frac{9\pi \cdot \mu \cdot D_O^3 \cdot Stk_C}{4 \cdot \rho_p \cdot Q \cdot C_C(P)} \right)^{0.5} \tag{1}$$

where μ is the dynamic viscosity of the gas, D_O is the diameter of the orifice, Stk_C is the critical Stokes number (0.24 for a circular orifice), ρ_p is the mass density of the particle material (i.e. silicon), Q is the volumetric flowrate through the orifice, and $C_C(P)$ is the Cunningham slip correction factor, which is dependent on pressure. Particles were assumed to stick to the QCM surface since the particles were small (< 10 nm) and thus the particles had a smaller kinetic energy in comparison to the adhesion energy [32, 33]. Particle size was verified using a transmission electron microscope (TEM), and results can be found in Sect. S.2 of the SI. To maintain constant impaction conditions, the orifice was cleaned between experiments using sonification in water for 5 min followed by blasting with pressurized air. The orifice was subsequently dried in a desiccator oven.

The quartz crystal was held by a sensor head (Telemark) equipped with a shutter. The resonance frequency of the quartz crystal was monitored using an OSC-100 oscillator (Inficon) and an FTM-2400 quartz crystal monitor (Kurt J. Lesker). The change in resonance

frequency of the quartz crystal can be converted into a mass loading by using the Sauer-brey equation [34]:

$$\Delta m = -\Delta f \cdot \left(\frac{A \cdot (\rho_q \cdot \mu_q)^{0.5}}{2 \cdot f_0^2} \right) \tag{2}$$

where Δm is the change in the mass loading of the quartz crystal, Δf is the change in the quartz crystal resonance frequency, A is the effective crystal area, ρ_q is the density of the quartz crystal (2.65 g cm^{-3}), μ_q is the shear modulus of the quartz crystal (2.95 10^{11} g cm^{-1} s^{-2}), and f_0 is the resonant frequency of the fundamental mode of the quartz crystal (6 MHz). To avoid overloading, the quartz crystal was replaced whenever $\Delta f > 40$ Hz from its original value. The sampling procedure for the QCM is as follows: plasma ignition, opening the QCM shutter after 10 s, particle sampling for up to 120 s, closing the QCM shutter, turning the plasma off. Deposition rates were determined by fitting the linear response of the QCM. Deposition rates were then converted into particle mass densities by normalizing the deposition rates by the volumetric flowrate to the QCM.

Particles were impacted onto a small area at the center of the crystal. As a result, the calculated mass loading is expected to be overestimated by a constant factor if the effective crystal area is assumed to be that of the overlapping electrodes on the quartz crystal (0.33 cm^2, as determined from the electrode geometry shown in Fig. S.3 of the SI). This overestimate is due to the quartz crystal having a radially dependent mass sensitivity, with a maximum sensitivity at the center [34–36]. To account for this effect, the sensitivity of the QCM was determined as a function of radial distance from the center of the quartz crystal, r. To perform this calibration, a 200 ng μL^{-1} solution of < 25 nm TiO$_2$ nanoparticles (Sigma-Aldrich, catalog number 637254) in deionized water (18.2 MΩ cm) was prepared. QCM sensitivity as a function of r was determined by depositing 0.2 μL of the prepared solution at various locations for a series of quartz crystals. The water was left to evaporate at atmospheric conditions for 6 min, leaving behind a deposit of TiO$_2$ nanoparticles of a known mass. QCM sensitivity was then calculated as the change in the quartz crystal resonance frequency over the mass loading. The positions of the deposits were measured from digital images of the quartz crystals. To avoid depositing over existing deposit and to simplify image processing, up to 4 depositions were performed in a line for each quartz crystal.

Downstream of the QCM, a quadrapole mass spectrometer (ExTorr Inc., Model XT300) was used to determine the amount of remaining silane. Ionization of the silane was performed by electron impact using an electron energy of 70 eV and a current of 2 mA. The $m/z = 31$ peak (corresponding to the mass-to-charge ratio of SiH$_3^+$, a dominant product of dissociative ionization of SiH$_4$) was normalized by the $m/z = 4$ peak (corresponding to helium) to account for small fluctuations of the reactor pressure upon plasma ignition and termination, which directly affected the flow to the mass spectrometer.

Computational Methods

GlobalKin, a 0-dimensional plasma chemistry model, was adapted for use in this work to predict NP growth. A detailed description of *GlobalKin* can be found in Refs. [37] and [38]. *GlobalKin* provides a volume averaged description of a plasma reactor by accounting for electron impact reactions, heavy particle reactions, surface reactions, and gas flow. Species densities are solved by integrating their continuity equations while

accounting for sources and losses due to gas flow, diffusion to surfaces, and reactions with electrons, ions, and neutrals. An average electron temperature is given by the electron energy equation. The master equation for the density of species i is

$$\frac{dn_i}{dt} = \sum_j \left\{ \left(a_{ij}^P - a_{ij}^R \right) k_j \prod_l n_l^{a_{ij}^R} \right\} + \sum_m \left\{ -\frac{D_i n_i}{\Lambda^2} f_m S_{im} + \sum_k \frac{D_k n_k}{\Lambda^2} f_m S_{km} g_{ikm} \right\} \quad (3)$$

where the first sum is over reactions j having rate coefficient k_j and l reactants. The stoichiometric coefficient for reactant species i in reaction j is a_{ij}^R and for products is a_{ij}^P. The second summation accounts for reactions on m different surfaces each having a fraction f_m of the total surface area. The first term in brackets is for loss of species i having diffusion coefficient D_i, diffusion length Λ and sticking coefficient S_{im} on surface m. The second term is for gain in species i due to reactions on the surface of species k with branching ratio to produce species i of g_{ikm}.

The conditions for the model are those of the experiment—a 52 sccm Ar/He/SiH$_4$ mixture flowing into a quartz tube reactor (diameter = 1.0 cm − 3.2 cm). Gas flow through the reactor is approximated using a plug-flow approach such that a slug of gas travels down the length of the reactor (15 cm) with an initial speed dependent upon inlet flowrate, gas density, and cross-sectional area of the reactor. The flow speed is adjusted as electron impact, heavy particle reactions, and gas heating change gas density to maintain a constant pressure. The power density profile is specified to approximate that of the experiment with a volume integral of the power density being held constant at 5 W.

A particle growth algorithm was incorporated into *GlobalKin* to investigate trends in Si NP growth and suppression as functions of plasma operating conditions. A list of species and reactions used in the model for NP growth are in S.8 of the SI. Briefly, silane molecules undergo electron impact dissociation to form Si$_x$H$_y$ radical species. A radical species is any Si$_n$H$_m$ species where $m < 2n + 2$. Any species having $m = 2n + 2$ is a saturated silane species. Dissociation of silane molecules is produced by electron impact dissociative excitation and ionization, dissociative recombination, charge exchange, and excitation transfer from rare gas atoms. Si$_n$H$_m$ radicals combine with each other or with saturated molecules to form higher order Si$_n$H$_m$ species. This process continues until Si$_n$H$_m$ clusters become large enough to be classified as nanoparticles. Here we classified a nanoparticle to be any Si$_n$H$_m$ species with $n \geq 13$. For example, the reaction

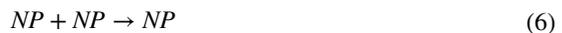$$Si_3H_7 + Si_{11}H_{24} \rightarrow NP \quad (4)$$

produces a NP as the sum of the silicon atoms in the reactants exceeds 12.

Nucleation reactions, as in Eq. (4), initially produce and increase both the mass density and number density of NPs. Surface growth reactions, such as

$$SiH_3 + NP \rightarrow NP \quad (5)$$

add to the mass density of NPs while not adding to the number density of NPs. Coagulation reactions such as

$$NP + NP \rightarrow NP \quad (6)$$

decrease the number density of NPs while not changing the mass density, thus yielding particles with larger effective radii. Neutral NPs were classified as being saturated or radicals, depending on the growth species.

The choice to represent a NP as any Si_nH_m species having greater than 13 Si atoms was based in part on computational efficiency and part on the concept of "critical cluster size." As higher order Si_nH_m species are included in the mechanism, the number of reactions needed—and therefore the computational time required—to account for nucleation and coagulation grows rapidly. Here we take "critical cluster size" to mean the point at which a particle has reached a sufficiently large radius that growth is dominated by surface processes (silane radicals sticking on the growing NP) and later by coagulation reactions (NP reacting with NP). Once the silane radicals have been depleted, growth is dominated by coagulation. The cross sections for both radical growth and coagulation increase as the number of Si atoms in the particle increases [39]. Optimization of the reaction mechanism used here has shown that the choice of 13 Si atoms to a NP enables representation of nucleation, growth and coagulation processes with relative computational efficiency on the timescales relevant in this system. This cluster size is consistent with experimental measurements of the smallest observable Si cluster by differential mobility analysis [40]. Nucleation, growth, and coagulation reactions occur simultaneously, though we expect the rate of coagulation to dominate as particles increase in size and silane radicals are depleted.

When nanoparticle number density in the plasma is high, they can carry both negative and positive charge [41, 42]. Negative and positive nanoparticles are accounted for as separate species with independent mass densities. Negative and positive nanoparticles can interact with neutral nanoparticles through charge exchange or coagulation, or with each other through neutralization reactions. We assume that the elementary charge on the particles does not exceed ±1. Previous work has shown that this assumption is valid when the nanoparticle diameter is small [43].

Particle growth is tracked by accounting for changes in particle mass density,

$$\frac{d\rho_m}{dt} = \sum_{i,j} n_i n_j k_{ij} \left(\pm \Delta m_{ij} \right) \tag{7}$$

where ρ_m is the instantaneous mass density of particle species m, k_{ij} is the reaction rate coefficient between species i and j having densities n_i and n_j. Δm_{ij} is the change in mass of the NP due to these reactions. Losses in particle mass density due to diffusion to the reactor walls are also accounted for (Eq. 3).

The instantaneous NP mass is derived from the mass density as

$$m_i = \frac{\rho_i}{n_i} \tag{8}$$

where n_i is the number density of NP particle species i. Assuming particles are spherical, the radius of the particle scales as

$$r_i = r_0 \left(\frac{m_i}{m_0} \right)^{1/3} \tag{9}$$

where r_0 is the original radius of the particle species and m_0 is the original mass of the particle species.

Scaling of NP Nucleation and Growth

Experiments were performed to validate the QCM impactor and to determine the effects of system parameters on particle formation. Qualifying the QCM impactor included verifying that the QCM could detect the onset of particle formation and calibrating the QCM to accurately relate the QCM response to mass loading. Following verification of the QCM impactor, the effects of pressure, hydrogen content, reactor tube diameter, and the silane fraction at the reactor inlet on particle formation were investigated using both experimental and computational methods.

Verification of the QCM Impactor

Preliminary validation of the QCM impactor, and establishing a nucleation threshold silane inlet fraction, were performed by tracking Δf over time while varying the fraction of silane fed into the plasma reactor around the nucleation threshold, as shown in Fig. 2. The expectation is that below the particle nucleation threshold, no mass deposition will be observed, as indicated by negligible change in the sensor resonance frequency. Above the threshold, a disproportionately large linear slope will be observed when compared to the silane inlet fraction below threshold. Very little to no particle deposition was observed up to a reactor inlet silane fraction of 140 ppm. However, particle deposition was observed at a silane inlet fraction of 174 ppm, indicated by the linear shift of the quartz crystal resonance frequency that is larger in magnitude than the digital noise floor. This result establishes a baseline that a minimum silane concentration at the reactor inlet is required for particles to nucleate and be detected [44, 45].

Since the resolution of the QCM is 0.1 Hz and instrumental drift is low (< 0.1 Hz min^{-1}), particles were said to be observed if $\Delta f/\Delta t > 0.3$ Hz min^{-1}. The reactor inlet silane fraction required to satisfy this criterion is defined as the nucleation onset fraction. Although this definition ignores potential particle losses upstream of the QCM, and variation in particle transmission efficiency due to distributions in particle size, it does account for the abrupt jump of $\Delta f/\Delta t$ observed over a relatively small change in silane feed fraction. A geometric description of the gas line from the plasma reactor to the QCM impactor orifice is provided in section S.4 of the SI.

Fig. 2 The change in the quartz crystal resonance frequency over time for various molar fractions of silane fed into the plasma reactor. The following parameters were used: reactor pressure: 6.5 Torr, tube diameter: 1.7 cm, and balance gas: spure Ar
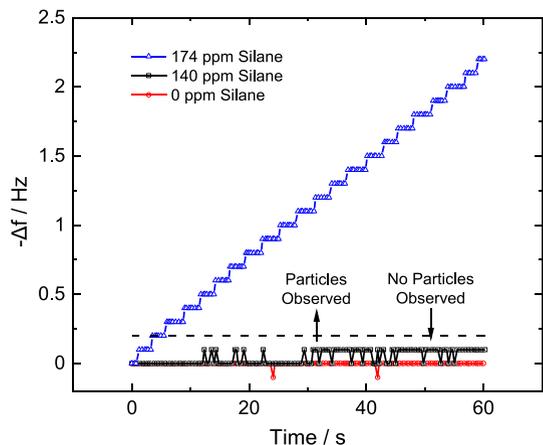
To accurately relate the change in frequency of the QCM to a mass loading, quartz crystal sensitivity (defined as $S = -\Delta f / \Delta m$) as a function of r was determined as shown by Fig. 3. Bessel functions and modified Bessel functions have been shown to accurately model the radially-dependent vibrational response of planar quartz crystals [35]. However, Eq. (10), an empirical relationship reported in the literature [46, 47], provided a more accurate description of the data. Note that similar expressions are used for plano-convex crystals [35]. A comparison of the two models can be found in Sect. S.3 of the SI.

$$S = S_{max} \cdot \exp(-\beta \cdot r^2) \qquad (10)$$

S_{max} represents the maximum sensitivity of the quartz crystal (where $r=0$), and β is an empirical constant which describes the width of the sensitivity distribution. Values for S_{max} and β were determined to be 3.40 Hz ng^{-1} and 73 cm^{-2} respectively. The area-averaged sensitivity of the quartz crystals was determined to be 0.28 Hz ng^{-1} using Eq. (11),

$$S_{avg} = \frac{2}{r_0^2} \int_0^{r_0} S(r) \cdot r \cdot dr \qquad (11)$$

where r_0 is the radius of the exposed quartz crystal (0.405 cm). From taking the ratio of S_{max} to S_{avg}, sensitivity of the quartz crystal is increased by a factor of 12 when depositing on the center of the quartz crystals rather than over the entire area. These sensitivities can also be converted into a minimum mass deposition rate required for detection by the QCM impactor of 88 pg min^{-1} for the center of the quartz crystal and approximately 1056 pg min^{-1} when depositing over the entire exposed area.

The Effects of System Parameters on Particle Formation: Experimental

To relate the nucleation onset fraction to experimental parameters, particle mass density (the mass deposition rate normalized by the volumetric flowrate to the QCM) was determined as a function of the silane fraction in the reactor inlet, reactor pressure, and hydrogen content, as shown in Fig. 4. For all cases, the mass density increased with increasing silane fraction at the reactor inlet. Intuitively, as more silane was fed into the reactor, more mass can be incorporated into particles. As pressure was increased at the same fraction

Fig. 3 Sensitivity of the quartz crystal, S, as a function of radial position, r. The dotted line represents the fit given by Eq. (10), and the error bars represent the area over which the deposit was spread. The maximum and area averaged sensitivities are provided
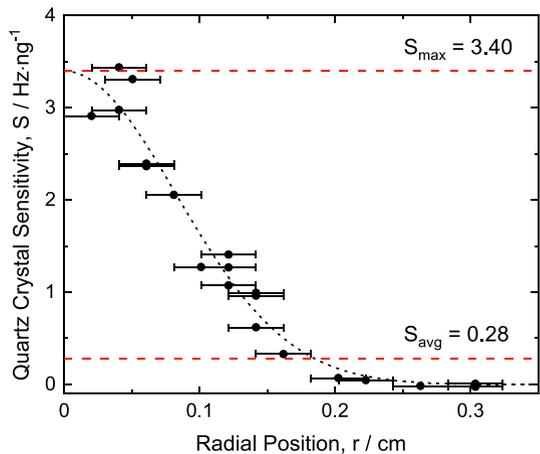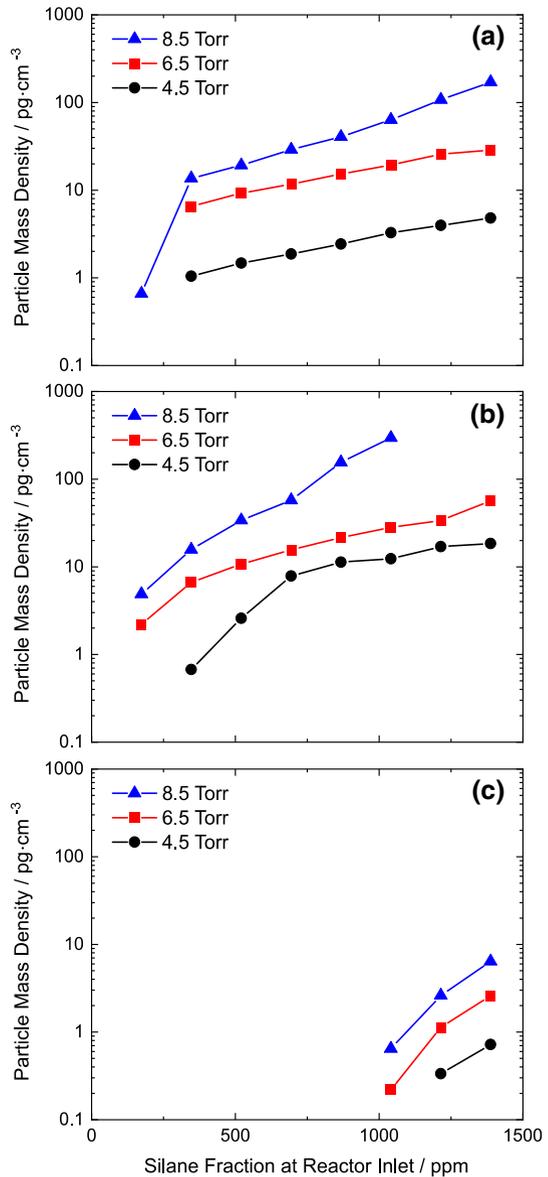
Fig. 4 Particle mass density as a function of the silane fraction fed into the plasma reactor for various pressures given a balance gas of **a** pure Ar, **b** 10% H_2 in Ar, **c** pure H_2. Tube diameter was held constant at 1.7 cm. Tabulated parameters and results are provided in section S.5 of the SI

of silane at the reactor inlet, particle mass density increased for all cases. The increase in mass density of the NPs agrees with the hypothesis that decreasing the diffusion coefficient of reactive silane radical species (by increasing the pressure) promotes particle formation over film deposition on the walls of the reactor. As the diffusion coefficient of reactive species is decreased and the reactor size is held constant, more radical species can be incorporated into particles before depositing on the walls since transport to the reactor walls is limited. Note that by the ideal gas law, increasing pressure will increase the silane mass density at the reactor inlet even if the fraction is the same. However, the pressure effects are

still significant if Fig. 4 is replotted as a function of silane mass density at the reactor inlet rather than silane fraction (see Sect. S.6 of the SI).

When a 10% H_2 gas mixture was used in the inlet, shown by Fig. 4b, particle mass density generally increased compared to the pure argon case, shown by Fig. 4a. This result was surprising as hydrogen has been reported to suppress particle formation [14, 17]. A moderate amount of H_2 in the balance gas appears to be disproportionately inhibiting film formation on the walls over particle growth for these conditions. Hydrogen radicals can deprotonate silane and other silyl species via hydrogen abstraction [48, 49], and the resultant faster reaction kinetics are expected to promote particle formation over film growth due to diffusion to the walls.

This mechanism would require the increased rate of silane deprotonation by hydrogen radicals to be greater than the increase in conversion of reactive silyl species back into silane by hydrogen incorporation. Alternatively, a small to moderate amount of H_2 in the inlet flow may disproportionally inhibit film formation over particle formation by reducing the number of potential reactive sites on the reactor walls. Upon increasing the hydrogen fraction from 10% H_2 to pure H_2, particle mass density in the effluent was decreased by over an order of magnitude (Fig. 4b, c). Particle formation is suppressed for high fractions of hydrogen in the balance gas. This effect will be later discussed in more detail.

Since the suppression of particle formation is important for a variety of industrial processes, the nucleation onset fraction was measured as a function of pressure and hydrogen content in the balance gas. The results are shown by Fig. 5. The nucleation onset fraction provides a minimum reactor inlet silane fraction above which particles can be detected with the QCM impactor. As the reactor pressure was increased, the nucleation onset fraction generally decreased. The effect of pressure was most significant when the balance gas was 10% H_2 where the nucleation onset fraction was reduced by a factor of 3 over a pressure range of 4.5 Torr to 8.5 Torr. However, this reduction was small considering that the increase in pressure results in an increase of the density of silane at the rector inlet by approximately a factor of 2. When a balance gas of pure H_2 was used, the nucleation onset fraction was larger and nearly constant over the pressure range that was investigated.

When the balance gas was switched to pure H_2, particle formation was greatly suppressed, as shown by Figs. 4c, 5. This result corroborates previous reports in the literature [14, 17], and can be explained by the suppression of silane conversion into reactive species. Mass spectroscopy was performed for verification, as shown in Fig. 6. For the pure

Fig. 5 The nucleation onset fraction of silane as a function of reactor pressure for various balance gases. The reactor tube diameter was 1.7 cm. The bottom and top of the error bars represent the reactor inlet silane fractions at which the measured deposition rate was below and above the nucleation threshold respectively
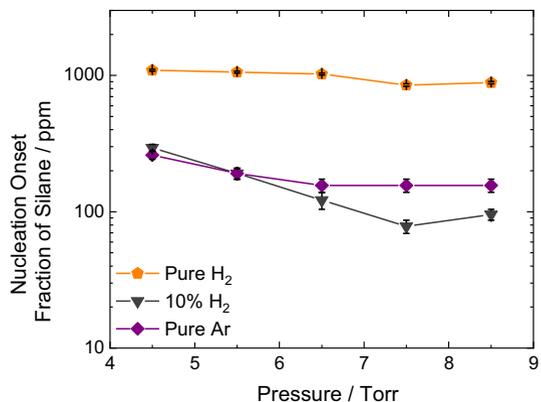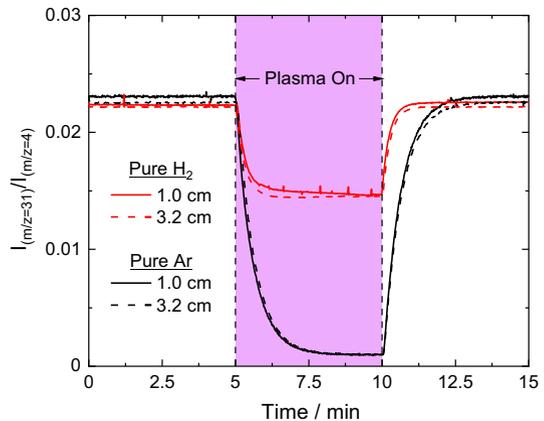
Fig. 6 Mass spectroscopy results showing the $m/z=31$ intensity (silane) over the $m/z=4$ intensity (helium) as a function of time given a balance gas of pure Ar or H_2. The silane feed fraction was 1388 ppm, the reactor pressure was 6.5 Torr. Two tube diameters were tested: 1.0 cm and 3.2 cm. Tabulated parameters and results are provided in section S.5 of the SI


Ar case, total silane conversion (into either particles or film on the walls) was over 95%. For the pure H_2 case, the total silane conversion was only 34%. As such, large fractions of hydrogen seem to aid in suppressing particle formation. However, there is a cost of also significantly reducing silane utilization.

Silane conversion was independent of tube diameter for 1.0 cm and 3.2 cm tubes at 6.5 Torr and otherwise the same flow conditions, as determined by mass spectroscopy of the plasma effluent (Fig. 6). The timescale of silane conversion is expected to be much shorter than the gas residence time in the plasma reactor [50], and the observed film deposition onto the reactor walls was consistent with that expectation, being largely located upstream or at the powered electrode with little film deposition past the grounded electrode (vide infra). As such, gas residence time, which changes with tube diameter at otherwise the same flow conditions, is not expected to be an important parameter in determining eluted particle mass density for our conditions. It would be ideal to have the capability to channel the silicon mass into either particle formation or film deposition, depending on the goal of the process, while maintaining a high precursor conversion. Varying reactor tube diameter appears promising to that end.

An interesting observation was made that the particle mass density increased with tube diameter, despite the conversion of silane being independent of tube diameter. To assess how the reactor tube diameter affects particle formation, particle mass density was measured as a function of the reactor inlet silane fraction at a constant reactor pressure of 6.5 Torr for various tube diameters, as shown by Fig. 7. Similar to the results shown in Fig. 4, particle mass density increased with increasing silane fraction at the reactor inlet for any given tube diameter. Upon increasing the tube diameter, particle mass density increased significantly for the pure Ar and 10% H_2 cases (over an order of magnitude when comparing the 1.0 cm tube mass densities to the 3.2 cm tube mass densities). These experiments were carried out at constant pressure and flow rate, and thus were free of artifacts due to changing silane mass density at the reactor inlet. This result is consistent with the original hypothesis that smaller tubes will suppress particle formation due to higher rates of diffusion loss to the walls. To further support the hypothesis, film deposition on the reactor walls was observed to increase for smaller tube sizes (noted by a much darker coloration on the reactor tube) as shown by Fig. 8. Each tube was subject to the same experimental conditions and methods (apart from the variable tube diameter). It is noted that

Fig. 7 Mass deposition rate as a function of the reactor inlet silane fraction fed into the plasma reactor for various tube diameters given a balance gas of **a** pure Ar, **b** 10% H_2 in Ar, **c** pure H_2. Reactor pressure was held constant at 6.5 Torr. Tabulated parameters and results are provided in section S.5 of the SI
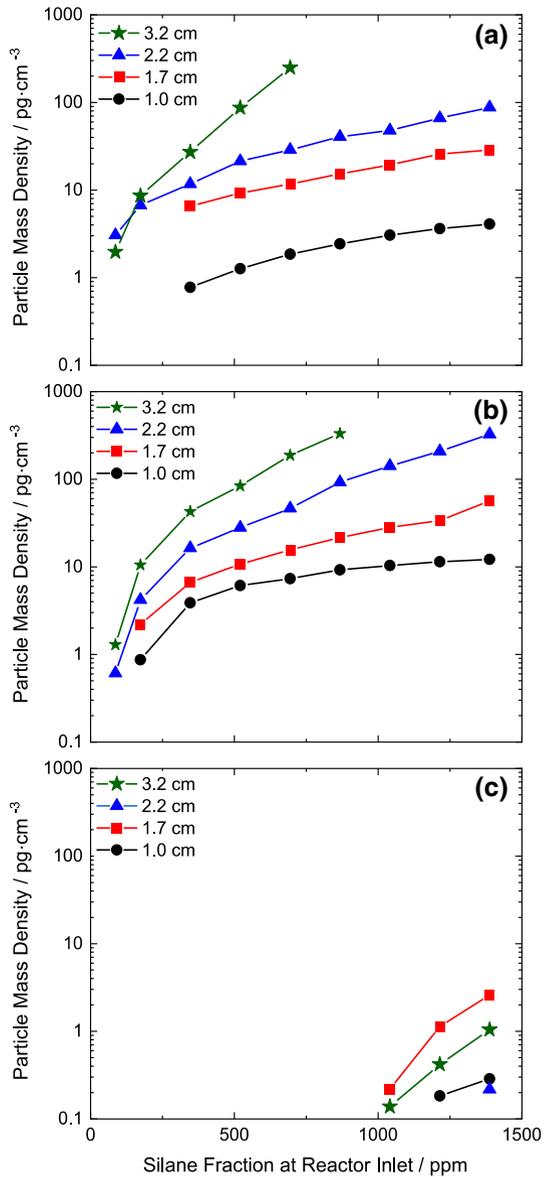
deposition was eventually observed for tubes of all sizes upon extended use, although the deposition was more rapid on smaller tubes (data not shown here).

Particle mass densities were similar for the cases when the balance gas was Ar compared to 10% H_2 (all else kept constant). However, when the balance gas was switched to pure H_2, a significant decrease in particle mass densities occurred. For the pure H_2 case, particle mass density no longer increased with increasing tube diameter. High H_2 content may be lowering reaction rates such that deposition on the reactor walls is limited by kinetics rather than diffusion. This would explain why particle formation was suppressed (due to

Fig. 8 Image of the silicon deposit on reactor tubes of various sizes. A 0.4 cm tube is included here to exaggerate tube diameter effects. Each tube was subjected to the same experimental conditions, apart from the changing tube diameter
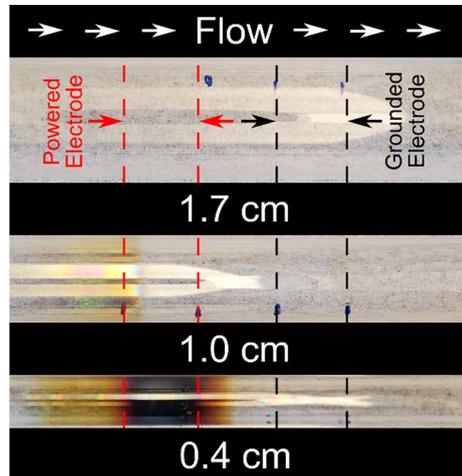

the lower concentrations of reactive species) and why the tube diameter becomes less relevant. As previously discussed, high H_2 content can suppress both particle and film formation on the walls of the tube. As such, the potential benefit of inhibiting particle formation is accompanied by reducing the film deposition rate.

The results shown in Fig. 7 indicate that increasing reactor tube diameter can increase particle mass density when the background gas is Ar, while with a balance gas of pure H_2, the particle mass density is nominally independent of tube diameter. It is not immediately clear how the nucleation onset fraction of silane will be affected. As such, it is useful to express the nucleation onset fraction of silane as a function of reactor parameters for applications which focus on inhibiting particle formation. The nucleation onset fractions as a function of tube diameter given a balance gas of pure Ar, 10% H_2, and pure H_2 are shown in Fig. 9. For the pure argon case, increasing the tube diameter from 1.0 to 3.2 cm decreases the nucleation onset fraction by over an order of magnitude, a result explained by diffusion losses to the wall.

Upon switching to a balance gas of 10% H_2, increasing the tube diameter from 1.0 to 3.2 cm only decreased the nucleation onset fraction by a factor of 2, as hydrogen can

Fig. 9 The nucleation onset fraction of silane as a function of reactor tube diameter for various balance gases. The reactor pressure was 6.5 Torr. The bottom and top of the error bars represent the reactor inlet silane fractions at which the measured deposition rate was below and above the nucleation threshold respectively
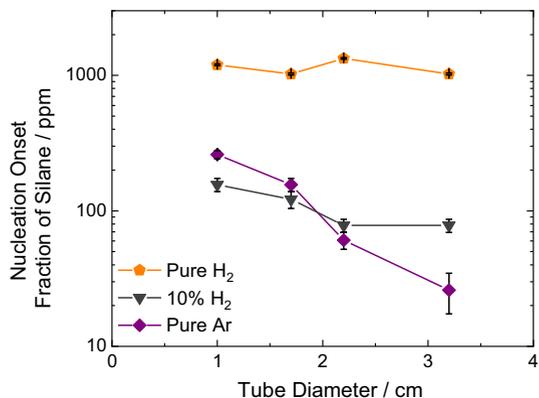
suppress the effects of varying tube diameter by limiting reaction kinetics. This result may suggest that the deprotonation of silane radical species by hydrogen radicals was not significant compared to the insertion of hydrogen to convert reactive silane species back into silane species. As such, hydrogen may generally inhibit silane conversion, but disproportionally favor particle formation or film formation depending on the specific reactor conditions.

The nucleation onset fraction was significantly increased when the balance gas was switched to pure H_2, meaning particle nucleation was suppressed. The nucleation onset fraction appears to be largely independent of the tube diameter for a pure H_2 balance gas. Although varying H_2 content and varying the tube diameter appear to be useful parameters for suppressing or promoting particle formation, these effects cannot be combined to suppress particle formation. Although hydrogen may be required for some deposition processes to control film crystallinity [15, 16], for processes that do not require hydrogen, the use of small reactor sizes for deposition processes shows promise for inhibiting particle formation.

The Effects of System Parameters on Particle Formation: Modelling

The computer model *GlobalKin* was used to further investigate the effects of changing reactor operating conditions on the nucleation and growth of silicon nanoparticles. The inlet gas mixture was flowed at 52 sccm with a small fraction (70–1000 ppm) of silane in argon through tubular reactors having varying diameters (1.0 cm, 1.7 cm, 2.2 cm, and 3.2 cm). The total RF power deposited and the pressure were held constant for all cases (5 W and 6.5 Torr).

The simulated mass densities and particle radii for the neutral NP (which had the largest density) as a function of inlet silane fraction are shown in Fig. 10 for all reactor diameters. The reactor outlet at which point these measurements were made is located 15 cm downstream of the inlet and 10 cm downstream of the power deposition region. The experimental sampling site is 60–61 cm further downstream. NP losses occurring in the sampling line that connects the plasma reactor to the QCM and the collection efficiency of the QCM have not been accounted for in the model. The model results are a measure of the maximum NP production rates and expect to closely track the experimental measurements downstream.

The general trends from the model closely match the experimental results of increasing mass density with increasing silane fraction. For all conditions, silane was converted to reactive precursor species within a few cm of the flow entering the power deposition zone, allowing for particle nucleation to rapidly begin. This observation is consistent with the results shown in Fig. 9 which suggests that onset of nucleation occurs at an inlet fraction of 200 ppm of silane or less in pure argon for all reactor sizes. In nearly all cases, silane consumption exceeded 95%.

These results suggest that NP growth is reaction limited and transport dominated. Particle number density at the outlet is higher for low silane inlet fractions than with large silane fractions. Inlet silane is depleted at roughly the same rate regardless of inlet silane fraction across all cases at the same reactor diameter. Nanoparticle number density increases in the plasma with increasing silane inlet fraction. However, at midrange silane inlet fractions (200 ppm for the 3.2 cm case) nanoparticle number density decreases downstream of the plasma as particles reach a critical cluster size and coagulate to form larger particles.

The model tracks a sequence of higher silane species and a single NP species, and the mass and radius of the NP species is calculated. Aside from the Si that may stick on the

Fig. 10 Particle mass density
(**a**) and radius (**b**) predicted by
GlobalKin as a function of silane
inlet fraction in argon for differ-
ent reactor diameters
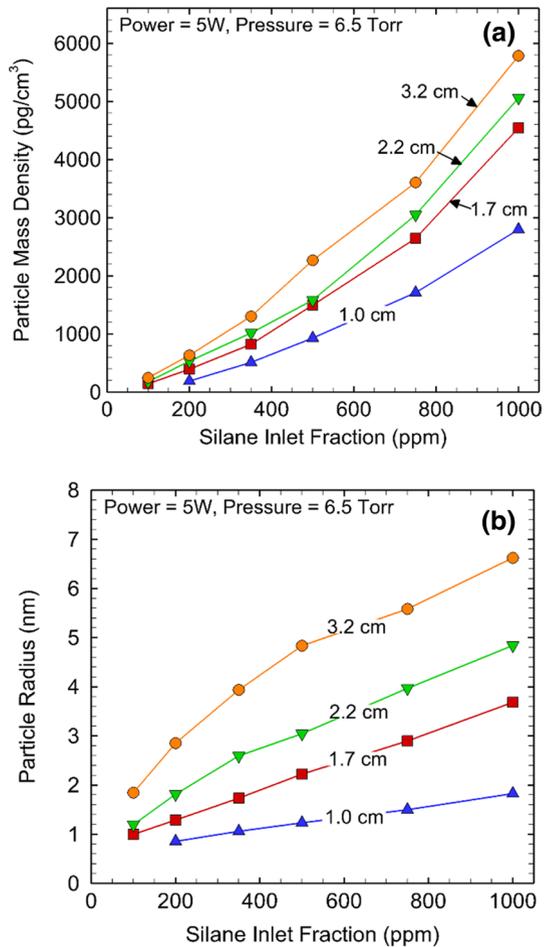
walls, the total mass (number) of Si atoms is conserved as a function of position. The dis-
tribution of that mass can be, for example, a larger number density of smaller NPs or a
smaller number density of larger NPs. As long as there is a flux of silane radicals nucleating
NPs at the smallest radius, the number density of NPs increases while keeping the average
size of the NP small. Once nucleation (the creation of new NPs) ceases due to the depletion
of nucleating radicals, growth of NPs is dominated by coagulation (NP + NP → NP), which
reduces the number of NPs while increasing the radius of the remaining NP to conserve the
total mass of Si. These processes are occurring simultaneously—though one process can
dominate over another.

In the low silane inlet fraction cases, the number density of particles downstream
remains high, and their size is small. This indicates that the dominant process adding mass
to the NPs is nucleation. Nucleation will increase the particle number density by continu-
ally supplying small particles to the system while coagulation will decrease the number
density as particles combine to create larger particles. The particle size does increase
somewhat, and that increase in NP diameter can be attributed primarily to coagulation.
These results for the low silane inlet fraction cases suggest particles are unable to grow

large enough for coagulation to dominate, meanwhile reactive precursors are lost to the wall or swept from the reactor by fluid flow.

A comparison of particle mass densities and radii across all reactor diameters at constant silane inlet fraction reinforces this observation. As reactor diameter decreases at constant inlet flow rate and pressure, the speed of the plug moving down the reactor increases. For comparison, the estimated plug speed in the 1.0 cm diameter reactor is about 150 cm/s whereas the estimated plug speed in the 3.2 cm reactor is 14 cm/s. The mass density of particles in all 3.2 cm cases is 2–3 times that in the 1.0 cm cases (3600 pg/cm^3 in the 3.2 cm reactor and 1700 pg/cm^3 in the 1.0 cm reactor at 500 ppm, for example). Due to the high rate of fluid flow in the 1.0 cm case, silane spends less time in the plasma region. However, the power deposition increases at the same rate, resulting in about the same dissociation fraction as in the 3.2 cm case. However, as noted above, decreasing the reactor diameter also decreases the effective diffusion length to the walls. Modelling results suggest that particle growth can be suppressed by decreasing reactor diameter or by decreasing silane inlet fraction, consistent with the experimental results. Film formation is most likely suppressed by increasing reactor size and adjusting silane inlet fraction above the nucleation threshold to achieve a target particle size.

To demonstrate the potential consequences of sticking coefficients to the reactor walls, which is a way of adjusting diffusional losses of reactive species to the boundary of the system, on nucleation and growth rates of particles in the plasma and gas phases, two extremes were simulated with the model—a small tube (1 cm diameter) with zero and unity sticking coefficients for all radicals, and a large tube (3.2 cm diameter). The reactor conditions are a constant flow rate of 52 sccm, 5 W, 6.5 Torr and 350 ppm SiH$_4$. The results for particle mass density and particle radius as a function of reactor position are shown in Fig. 11. For a diameter of 1 cm, there is a significant increase in particle radius and particle mass density from a sticking coefficient, $s=1$ to $s=0$. For a diameter of 3.2 cm, there is little change in particle radius for the same change in sticking coefficient. The particle mass density increases with decreasing sticking coefficient, though less appreciably in the 3.2 cm case compared to the 1.0 cm case. For a diameter of 1.0 cm, the more rapid rate of radical loss to the walls with $s=1$, even with a smaller residence time, results in lower net growth rates, smaller particles, and lower total particle mass density. For a diameter of 3.2 cm there is little change in the particle diameter between $s=0$ and $s=1$ as volumetric processes are dominating the number densities of particle precursors and growth species in the plasma zone. However, downstream, after nucleation has occurred for both cases, the $s=0$ case produces a larger number density of smaller particles due to growth reactions of radicals onto the particles dominating over coagulation.

Conclusions

In this work, a QCM impactor has been shown to be a promising method for sampling aerosolized particles (of sizes below 10 nm) under vacuum conditions at low mass densities. By depositing particles on the center of a QCM crystal, rather than over the entire area, device sensitivity was shown to increase by over an order of magnitude. Using this QCM impactor, particle mass densities from the effluent of a dilute silane plasma were measured. These mass densities were determined as a function of the inlet silane fraction, gas composition, reactor pressure, and reactor tube diameter. Increasing the reactor tube diameter was shown to significantly increase particle mass density, and increasing the reactor pressure

Fig. 11 Particle properties for varying sticking coefficients. **a** Particle radius and **b** mass density for tube diameters of 1.0 and 3.2 cm for two cases of the sticking coefficient for all silane radical species, $s=0$ and $s=1$
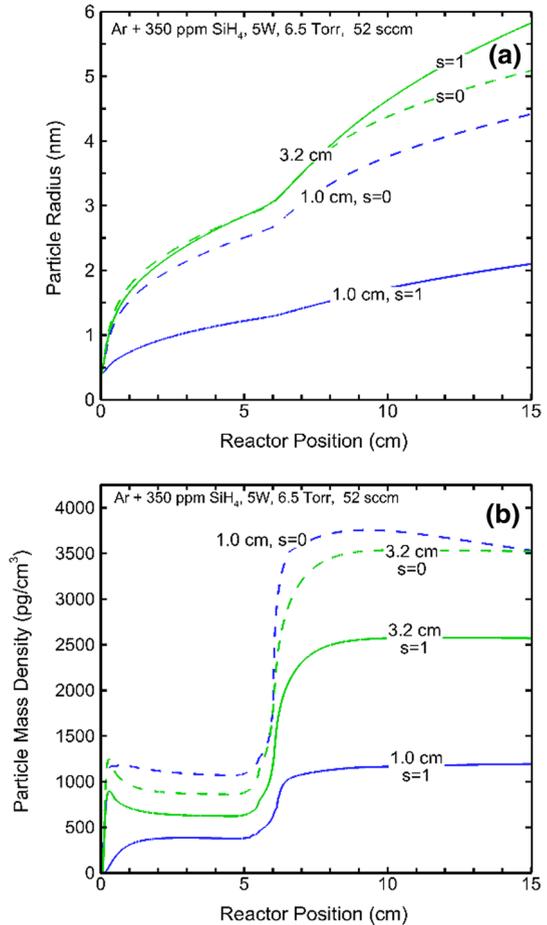
was also shown to increase particle mass density. Particle formation was greatly inhibited when pure H_2 was used as the balance gas. These results suggest that species diffusion to surfaces that act as sinks (e.g. reactor walls) plays a major role in determining whether film formation is favored over particle formation. Reactor conditions having high hydrogen fraction suppresses both film formation, and to a greater extent, particle formation.

Experimental and modeling results indicate that diffusion of radicals and their loss on the walls can be important with respect to NP formation. When varying the sticking coefficient of silicon precursor species on the reactor walls in the model, we see similar dependencies with respect to the experiments. These dependencies could be sensitive functions of reactor radius as sticking coefficients are likely a function of reactor radius. Changes in sticking coefficient at the reactor walls would be expected as the walls are subject to heating, ion bombardment, and photo desorption over the life of the reactor. As a film is deposited on the walls, sticking coefficients may change. Further studies are needed to fully parameterize these dependencies. Results from the model suggest that controlling particle growth and film formation is a delicate balance between controlling the particle growth regime (nucleation vs. coagulation) and fluid properties. Additionally, the model results

suggest that reactor diameter (which also determines residence time for a given flow rate) should be tuned in combination with inlet gas composition to either achieve a particle-free film, or particles of a specified size while also suppressing film formation on the reactor walls.

Data Availability The processed data that support our conclusions are contained in this article. The raw data resulting from the simulations are available from the corresponding author upon reasonable request.

Declarations

Conflict of interest The authors declare no conflicts of interest.

References

1. Kang Z, Tsang CHA, Wong N-B, Zhang Z, Lee S-T (2007) Silicon quantum dots: a general photocatalyst for reduction, decomposition, and selective oxidation reactions. J Am Chem Soc 129:12090–12091. https://doi.org/10.1021/ja075184x
2. Lv P, Xu C, Peng B (2020) Design of a silicon photocatalyst for high-efficiency photocatalytic water splitting. ACS Omega 5:6358–6365. https://doi.org/10.1021/acsomega.9b03755
3. Ni Z, Zhou S, Zhao S, Peng W, Yang D, Pi X (2019) Silicon nanocrystals: unfading silicon materials for optoelectronics. Mater Sci Eng R Rep 138:85–117. https://doi.org/10.1016/j.mser.2019.06.001
4. Yang Y, Yuan W, Kang W, Ye Y, Yuan Y, Qiu Z, Wang C, Zhang X, Ke Y, Tang Y (2020) Silicon-nanoparticle-based composites for advanced lithium-ion battery anodes. Nanoscale 12:7461–7484. https://doi.org/10.1039/C9NR10652A
5. O'Farrell N, Houlton A, Horrocks BR (2006) Silicon nanoparticles: applications in cell biology and medicine. Int J Nanomed 1:451–472. https://doi.org/10.2147/nano.2006.1.4.451
6. Ksenofontova OI, Vasin AV, Egorov VV, Bobyl AV, Soldatenkov FY, Terukov EI, Ulin VP, Ulin NV, Kiselev OI (2014) Porous silicon and its applications in biology and medicine. Tech Phys 59:66–77. https://doi.org/10.1134/S1063784214010083
7. Cooper DW (1986) Particulate contamination and microelectronics manufacturing: an introduction. Aerosol Sci Technol 5:287–299. https://doi.org/10.1080/02786828608959094
8. Herrling MP, Rychen P (2017) Review of nanoparticles in ultrapure water: definitions and current metrologies for detection and control. Ultrapure Micro 1:34–43
9. Selwyn GS (1991) Plasma particulate contamination control. I. Transport and process effects. J Vac Sci Technol B Microelectron Nanometer Struct Process Meas Phenom 9:3487–3492. https://doi.org/10.1116/1.585829
10. Jellum GM, Daugherty JE, Graves DB (1991) Particle thermophoresis in low pressure glow discharges. J Appl Phys 69:6923–6934. https://doi.org/10.1063/1.347630
11. Kashihara N, Setyawan H, Shimada M, Hayashi Y, Kim CS, Okuyama K, Winardi S (2006) Suppression of particle generation in a plasma process using a sine-wave modulated rf plasma. J Nanoparticle Res 8:395. https://doi.org/10.1007/s11051-005-9005-1
12. Bouchoule A, Plain A, Boufendi L, Blondeau JPh, Laure C (1991) Particle generation and behavior in a silane-argon low-pressure discharge under continuous or pulsed radio-frequency excitation. J Appl Phys 70:1991–2000. https://doi.org/10.1063/1.349484
13. Watanabe Y, Shiratani M, Makino H (1990) Powder-free plasma chemical vapor deposition of hydrogenated amorphous silicon with high rf power density using modulated rf discharge. Appl Phys Lett 57:1616–1618. https://doi.org/10.1063/1.104087
14. Shiratani MSM, Maeda SMS, Koga KKK, Watanabe YWY (2000) Effects of gas temperature gradient, pulse discharge modulation, and hydrogen dilution on particle growth in silane RF discharges. Jpn J Appl Phys 39:287. https://doi.org/10.1143/JJAP.39.287

15. Kroll U, Meier J, Shah A, Mikhailov S, Weber J (1996) Hydrogen in amorphous and microcrystalline silicon films prepared by hydrogen dilution. J Appl Phys 80:4971–4975. https://doi.org/10.1063/1.363541

16. Matsuda A (1983) Formation kinetics and control of microcrystallite in μc-Si: H from glow discharge plasma. J Non-Cryst Solids 59–60:767–774. https://doi.org/10.1016/0022-3093(83)90284-3

17. Kim Y, Koga K, Shiratani M (2020) Effect of hydrogen dilution on the silicon cluster volume fraction of a hydrogenated amorphous silicon film prepared using plasma-enhanced chemical vapor deposition. Curr Appl Phys 20:191–195. https://doi.org/10.1016/j.cap.2019.11.001

18. Amor SB, Dimassi W, Tebai MA, Ezzaouia H (2012) Effect of the hydrogen flow rate on the structural and optical properties of hydrogenated amorphous silicon thin films prepared by plasma enhanced chemical vapor deposition. Phys Status Solidi C 9:2180–2183. https://doi.org/10.1002/pssc.201200238

19. Wang SC, Flagan RC (1990) Scanning electrical mobility spectrometer. Aerosol Sci Technol 13:230–240. https://doi.org/10.1080/02786829008959441

20. Keskinen J, Pietarinen K, Lehtimäki M (1992) Electrical low pressure impactor. J Aerosol Sci 23:353–360. https://doi.org/10.1016/0021-8502(92)90004-F

21. Marple VA, Rubow KL, Behm SM (1991) A microorifice uniform deposit impactor (MOUDI): description, calibration, and use. Aerosol Sci Technol 14:434–446. https://doi.org/10.1080/02786829108959504

22. Friedlander S (2000) Smoke, dust, and haze. Oxford University Press, Oxford

23. Hinds WC (1999) Aerosol technology: properties, behavior, and measurement of airborne particles. Wiley, New Jersey

24. Nash DG, Baer T, Johnston MV (2006) Aerosol mass spectrometry: an introductory review. Int J Mass Spectrom 258:2–12. https://doi.org/10.1016/j.ijms.2006.09.017

25. Hevroni A, Golan H, Fialkov A, Rahinov I, Tsionsky V, Markovich G, Cheskis S (2011) In situ measurement of the mass concentration of flame-synthesized nanoparticles using quartz-crystal microbalance. Meas Sci Technol 22:115102. https://doi.org/10.1088/0957-0233/22/11/115102

26. Fomin A, Poliak M, Rahinov I, Tsionsky V, Cheskis S (2013) Combined particle mass spectrometer – quartz crystal microbalance apparatus for in situ nanoparticle monitoring during flame assisted synthesis. Combust Flame 160:2131–2140. https://doi.org/10.1016/j.combustflame.2013.04.011

27. Maemura Y, Fujiyama H, Takagi T, Hayashi R, Futako W, Kondo M, Matsuda A (1999) Particle formation and a-Si: H film deposition in narrow-gap RF plasma CVD. Thin Solid Films 345:80–84. https://doi.org/10.1016/S0040-6090(99)00100-5

28. Bhandarkar U, Kortshagen U, Girshick SL (2003) Numerical study of the effect of gas temperature on the time for onset of particle nucleation in argon–silane low-pressure plasmas. J Phys Appl Phys 36:1399–1408. https://doi.org/10.1088/0022-3727/36/12/307

29. Uner NB, Thimsen E (2018) Low temperature plasma as a means to transform nanoparticle atomic structure. Plasma Sources Sci Technol 27:074005. https://doi.org/10.1088/1361-6595/aad36e

30. Lin Q, Lin X, Yu Y, Wang H, Chen J (1993) Measurements in silane radio frequency glow discharges using a tuned and heated Langmuir probe. J Appl Phys 74:4899–4902. https://doi.org/10.1063/1.354322

31. Orifice Calculator © Lenox Laser. https://lenoxlaser.com/resources/calculators/orifice-calculator/. Accessed 19 Oct 2021

32. Ihalainen M, Lind T, Arffman A, Torvela T, Jokiniemi J (2014) Break-up and bounce of TiO2 agglomerates by impaction. Aerosol Sci Technol 48:31–41. https://doi.org/10.1080/02786826.2013.852155

33. Ellenbecker MJ, Leith D, Price JM (1980) Impaction and particle bounce at high stokes numbers. J Air Pollut Control Assoc 30:1224–1227. https://doi.org/10.1080/00022470.1980.10465173

34. Sauerbrey G (1959) Verwendung von schwingquarzen zur wägung dünner schichten und zur mikrowägung. Z Für Phys 155:206–222. https://doi.org/10.1007/BF01337937

35. Cumpson PJ, Seah MP (1990) The quartz crystal microbalance; radial/polar dependence of mass sensitivity both on and off the electrodes. Meas Sci Technol 1:544–555. https://doi.org/10.1088/0957-0233/1/7/002

36. Josse F, Lee Y, Martin SJ, Cernosek RW (1998) Analysis of the radial dependence of mass sensitivity for modified-electrode quartz crystal resonators. Anal Chem 70:237–247. https://doi.org/10.1021/ac9706032

37. Lietz AM, Kushner MJ (2016) Air plasma treatment of liquid covered tissue: long timescale chemistry. J Phys Appl Phys 49:425204. https://doi.org/10.1088/0022-3727/49/42/425204

38. Goto N, Kudo S, Motoyama H, Ohyama S (2002) Direct decomposition technique for NO in O2–N2 mixture using barrier discharge and Cu zeolite. Jpn J Appl Phys 41:L64. https://doi.org/10.1143/JJAP.41.L64
39. Olevanov MA, Mankelevich YuA, Rakhimova TV (2004) Coagulation and growth mechanisms for dust particles in a low-temperature plasma. J Exp Theor Phys 98:287–304. https://doi.org/10.1134/1.1675896
40. Vazquez-Pufleau M, Wang Y, Biswas P, Thimsen E (2020) Measurement of sub-2 nm stable clusters during silane pyrolysis in a furnace aerosol reactor. J Chem Phys 152:024304. https://doi.org/10.1063/1.5124996
41. Gatti M, Kortshagen U (2008) Analytical model of particle charging in plasmas over a wide range of collisionality. Phys Rev E 78:046402. https://doi.org/10.1103/PhysRevE.78.046402
42. Agarwal P, Girshick SL (2012) Sectional modeling of nanoparticle size and charge distributions in dusty plasmas. Plasma Sources Sci Technol 21:055023. https://doi.org/10.1088/0963-0252/21/5/055023
43. Lanham SJ, Polito J, Shi X, Elvati P, Violi A, Kushner MJ (2021) Scaling of silicon nanoparticle growth in low temperature flowing plasmas. J Appl Phys 130:163302. https://doi.org/10.1063/5.0062255
44. Slootman F, Parent J-C (1994) Homogeneous gas-phase nucleation in silane pyrolysis. J Aerosol Sci 25:15–21. https://doi.org/10.1016/0021-8502(94)90178-3
45. Nijhawan S, McMurry PH, Swihart MT, Suh S-M, Girshick SL, Campbell SA, Brockmann JE (2003) An experimental and numerical study of particle nucleation and growth during low-pressure thermal decomposition of silane. J Aerosol Sci 34:691–711. https://doi.org/10.1016/S0021-8502(03)00029-6
46. Lin Z, Hill RM, Davis HT, Ward MD (1994) Determination of wetting velocities of surfactant superspreaders with the quartz crystal microbalance. Langmuir 10:4060–4068. https://doi.org/10.1021/la00023a026
47. Zhuang H, Lu P, Lim SP, Lee HP (2007) Frequency response of a quartz crystal microbalance loaded by liquid drops. Langmuir 23:7392–7397. https://doi.org/10.1021/la063767z
48. Agarwal P, Girshick SL (2014) Numerical modeling of an RF argon-silane plasma with dust particle nucleation and growth. Plasma Chem Plasma Process 34:489–503. https://doi.org/10.1007/s11090-013-9511-3
49. Le Picard R, Markosyan AH, Porter DH, Girshick SL, Kushner MJ (2016) Synthesis of silicon nanoparticles in nonthermal capacitively-coupled flowing plasmas: processes and transport. Plasma Chem Plasma Process 36:941–972. https://doi.org/10.1007/s11090-016-9721-6
50. Lopez T, Mangolini L (2014) On the nucleation and crystallization of nanoparticles in continuous-flow nonthermal plasma reactors. J Vac Sci Technol B 32:061802. https://doi.org/10.1116/1.4899206